Formate-Induced Dissolution and Reprecipitation of a Copper Electrocatalyst During Electrochemical CO_2 Reduction Reaction

Seunghoon Lee[1], Nishu Devi[1], Yuanyuan Li[1], Yiqing Wu[1], Barbara R. Evans[1], Matthew G. Boebinger[2], Chang Liu[1] Andrew G. Stack[1], Zili Wu[1,2], and Juliane Weber[*1]

[1] Chemical Sciences Division, Oak Ridge National Laboratory, Oak Ridge, TN, USA.

[2] Center for Nanophase Materials Sciences, Oak Ridge National Laboratory, Oak Ridge, TN, USA.

Draft of September 9th, 2025

Revisions for The Journal of Physical Chemistry C

Abstract

Catalyst size, morphology, and crystal structure play a crucial role in determining the activity and selectivity of electrochemical CO_2 reduction reactions, which are known to change during the reaction process. A comprehensive understanding of how, when, and why these parameters evolve under operational conditions is essential for developing stable, efficient, and selective catalysts. In this study, we reveal that formate, one of the reaction products, contributes to the degradation of copper catalysts through a ligand-assisted dissolution mechanism. Utilizing in-situ electrochemical atomic force microscopy and ex-situ scanning and transmission electron microscopy, we observed a significant reduction in the size of copper nanoparticles, which decreased from over 30 nm to less than 10 nm in diameter within 60 minutes of CO_2RR. The temporal production of formate correlated with the particle size changes. Furthermore, analysis of the electrolyte using inductively coupled plasma optical emission spectroscopy confirmed the dissolution of copper nanoparticles. Control experiments involving various reaction products (H_2, CO, and $HCOO^-$) demonstrated that formate significantly promotes copper dissolution, thereby highlighting its role in the ligand-assisted dissolution mechanism of copper electrocatalysts. Our findings provide critical insights

into coper catalyst behavior during electrochemical CO_2 reduction, facilitating the design of more resilient and effective electrocatalysts.

Introduction

The electrochemical CO_2 reduction reaction (CO_2RR) with renewably-sourced electrons is potentially a promising way to convert waste CO_2 into clean chemicals and value-added fuels such as ethylene and ethanol.[1] As an electrocatalyst, copper has been widely recognized as the only monometallic catalyst that can reduce CO_2 to multicarbon (C_{2+}) products.[2] Great progress has been made in understanding the parameters that govern its activity and selectivity,[3-5] but a fundamental understanding of its catalytic stability under reaction conditions is not complete, preventing the development of robust copper-based CO_2RR catalysts.

Common consensus about the dynamic change of copper electrocatalysts is based on intrinsic characteristic of copper such as its tendency of redox cycle and high surface mobility. Copper is easily oxidized by electrolyte contact (or air exposure during sample preparation), however, oxidized copper dissolves transiently and is reduced to metallic copper under a cathodic potential (e.g., — 1.0 V vs. reversible hydrogen electrode, RHE). Its Pourbaix diagram supports that copper exists in its metallic state across the entire pH window[6] and metallic copper is supposed to be stable at cathodic potentials used for CO_2RR.[7-10]

However, numerous studies have shown that the copper electrocatalyst undergo physical (e.g., morphology and crystal structure)[11-13] or chemical (e.g., oxidation or dissolution) change during the reaction,[14, 15] affecting product selectivity or distribution during the reaction. Several nanoscale degradation mechanisms are proposed in the literature: detachment, dissolution[16] and reprecipitation[14, 17, 18], Ostwald ripening[19], reshaping, fragmentation[12, 20], agglomeration[21] and poisoning[22]. Almost all degradation pathways result in morphological changes of copper catalysts which often show reconstruction of the copper crystal structure. New facets can appear[12]; for example, copper was found to undergo a transformation during CO_2RR from polycrystalline to Cu(100)[7].

Current consensus is that the morphological change of copper is related to its high surface mobility and interaction with chemical species such as *CO[23-25] (*represents the adsorbed state) an intermediate product formed during CO_2RR. Because of copper's low cohesive energy and high surface mobility, the copper atoms at the electrode surface can easily migrate and the adsorption of CO at copper sites with low coordination number can further lead to weakening of binding of copper to its neighboring atoms, resulting in decomposition into smaller sizes.[24] However, since the referenced studies employed single crystal copper and thin film structures of copper, it is premature to conclude that CO is the sole chemical species that can lead to morphological changes in all copper based catalysts. This is mainly because the binding energy of chemical species to copper varies depending on crystal facet, particle size and morphology[26, 27], which therefore could lead to different degradation mechanisms of single crystal facets and multi-faceted particles. Another common two-electron reduction product from CO_2RR is formate ($HCOO^-$) over copper catalysts. However, its role on the morphological evolution of copper catalysts during CO_2RR has been overlooked in the field.

In this study, we aim to reveal the mechanisms driving the copper catalyst degradation by tracking reaction products including both CO and formate, dissolved copper concentration in the electrolyte, and the size and morphology of the copper catalyst by combining in situ and ex situ approaches (including in situ electrochemical (EC) atomic force microscopy (AFM) (EC-AFM), in situ X-ray adsorption spectroscopy (XAS) and ex situ scanning electron microscopy (SEM) and transmission electron microscopy (TEM)) under CO_2RR. Our combined results suggest that formate, rather than CO, is the primary product that drives dissolution of the polycrystalline copper oxide nanoparticles and redeposition of small copper nanoparticles on the carbon support under our studied CO_2RR conditions.

Results and Discussion

1. Particle Morphology and Size Distribution

a. Catalyst Characterization before CO_2RR

To assess morphological changes in the copper electrocatalyst during CO_2RR, the size distribution of copper nanoparticle was characterized under different conditions: before any reaction and after

applying -1.0 V vs. RHE (V_{RHE}) for 1, 5, 10, and 60 minutes. Before the reaction, mean particle size was ~93 ± 32 nm measured by SEM image analysis (Figure 1 and 2A; images provided in Figure S1-S26). Median particle size was 85 nm ± 32 nm, with a minimum particle size of 35 nm and a maximum particle size of 217 nm. TEM image analysis of the copper particles before coating them on the electrode and reduction reaction showed a smaller mean particle size centered around 30 nm (n=100 particles) (Figure 1B and 1C). This indicates that the SEM analysis provides the aggregate size and not primary particle size, whereas TEM analysis provides primary particle size. High resolution TEM imaging showed twinning inside the copper particles, indicating polycrystalline particles (1D).

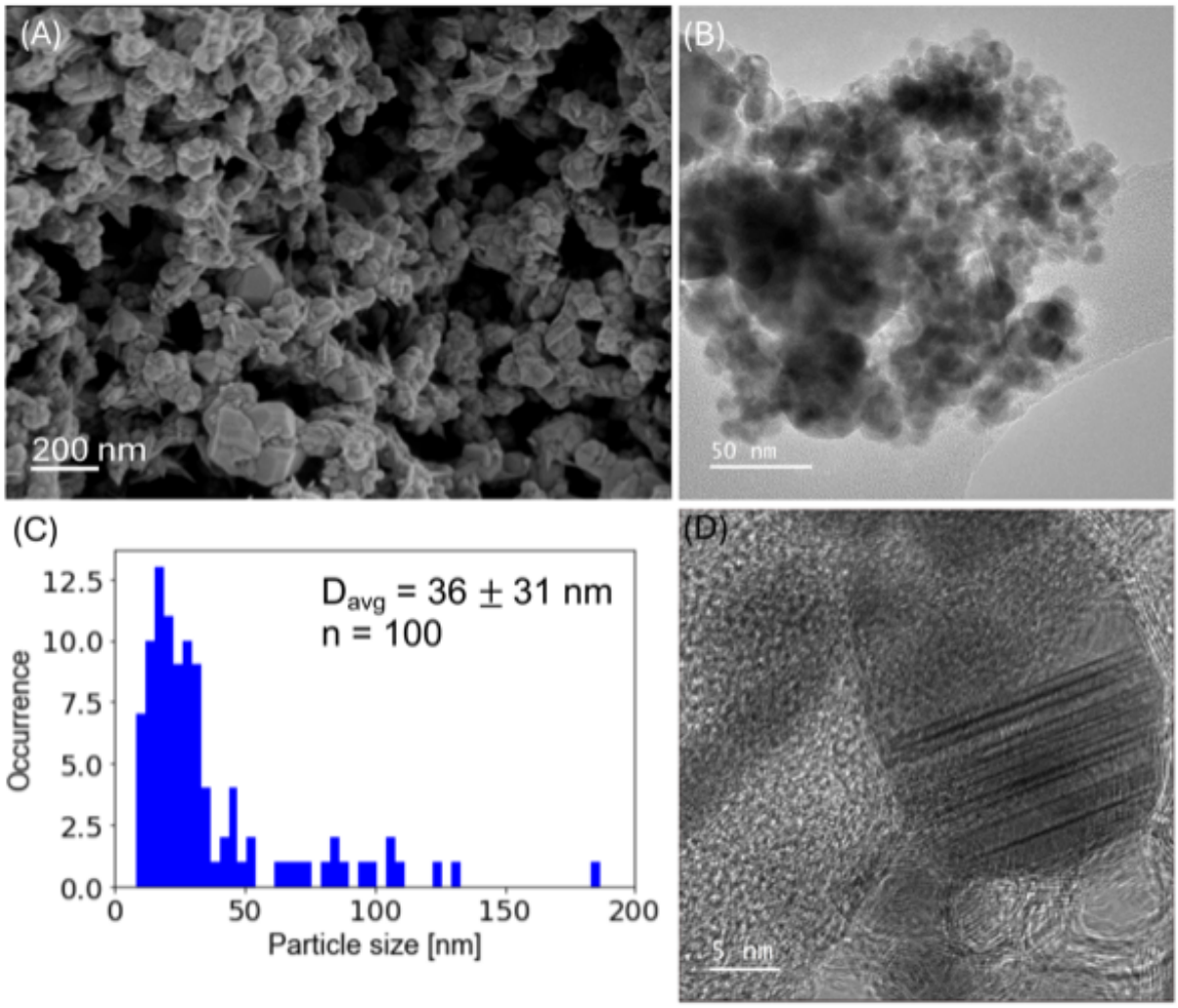

Figure 1 Morphological characterization of copper catalyst before CO_2RR. (A) Scanning electron microscopy image of copper particles. Partial oxidation of particles is visible. (B) Bright field transmission electron microscope (TEM) image of typical particles. (C) Particle size distribution obtained from TEM image analysis, number of analyzed particles (n): 100, mean diameter: 36 ± 31 nm. (D) Twinning in copper catalyst. Images analyzed to obtain particle size distribution are given in Figure S1-S26 and values in Table S1.

XAS analysis of copper catalyst coated on carbon paper using a binder showed a coordination number of 4.8 ± 0.4 for Cu-Cu (measured bond distance is 2.542 ± 0.002 Å, which matches well with literature values of 2.56 Å[28]) and 1.4 ± 0.2 for Cu-O (measured bond distance is

1.90 ± 0.01 Å, which matches well with literature value of 1.86 Å for Cu_2O[29]), indicating that some of the copper atoms were oxidized under ambient condition before the reaction.

b. Morphological Evolution During CO_2RR

The morphology of the copper nanoparticles significantly changed under the reductive potential (—1.0 V_{RHE}) compared to pre-reaction (Figure 2A-E; additional images given in Figure S32-S36). Post-reaction particle sizes were mostly characterized by ex situ SEM due to difficulties to separate particles from binder post reaction. While SEM analysis does not provide the primary particle size but the aggregate size, as discussed above, it should still provide qualitative information for the size changes of copper nanoparticles.

After 1 min reaction, mean particle size measured in SEM image analysis shifted significantly to 34 ± 32 nm, which is equal to a 63% reduction in size. Copper particle size after 1 min CO_2RR was also characterized using TEM/STEM imaging, where the mean measured particle size was 6.1 ± 7.7 nm (n = 170), which is equal to 83% reduction in size (Images given in Figure S27-31, values in Table S2). So, the trend observed by SEM and TEM imaging on copper nanoparticle size change is in general agreement upon CO_2RR. The median particle size measured by SEM decreased to 23 nm, with a minimum size of 1 nm and a maximum particle size of 140 nm. The median particle size measured by TEM decreased to 3.6 nm, with a minimum size of 0.2 nm and a maximum size of 46.3 nm.

The mean particle size continued to decrease until 10 minutes had elapsed, per SEM measurements. The mean diameter of the copper nanoparticles was 20 ± 22 nm after 5 min and 17 ± 18 nm after 10 min. The mean diameter of the copper nanoparticles was 21 ± 11 nm after 60 minutes reaction time. Further aggregation was observed after 90 and 120 minutes of reaction time (Figure S37) with a mean diameter of copper nanoparticles of 31 ± 34 nm after 90 minutes and 62 ± 27 nm after 120 minutes. The median particle size was 14 nm after 5 minutes of reaction time, 11 nm after 10 minutes reaction rate time, 19 nm after 60 minutes and 55 nm after 120 minutes. There is also a distinct change in minimum and maximum. For 5, 10, 60 minutes, the minimum particle size are 1, 1 and 3 nm. The maximum particle size for 5, 10, 60 minutes is 137 nm, 88 nm and 60 nm. Because the standard deviation for the SEM particle size analysis is high, we also

analyzed the particle size distribution (Figure 3F-J). The particle size distribution shows a clear shift in size distribution from the before CO_2RR sample to the 10 min sample which contain a larger proportion of particles <10 nm. All calculated values (mean, standard deviation, median, maximum and minimum) are given in Table S3 of the supporting information.

To ensure that our ex-situ SEM and TEM observations were representative, we conducted near identical location TEM. For these experiments, we utilized a pointer grid and analyzed copper nanoparticles prior to CO_2RR. We then conducted CO_2RR using the TEM grid as working electrode and analyzed copper nanoparticles after 5 minutes of CO_2RR. We observed typical copper nanoparticle morphology in our fresh catalyst (Figure 2). After 5 minutes of CO_2RR, newly formed small particles were visible (Figure 2), matching our SEM observations.

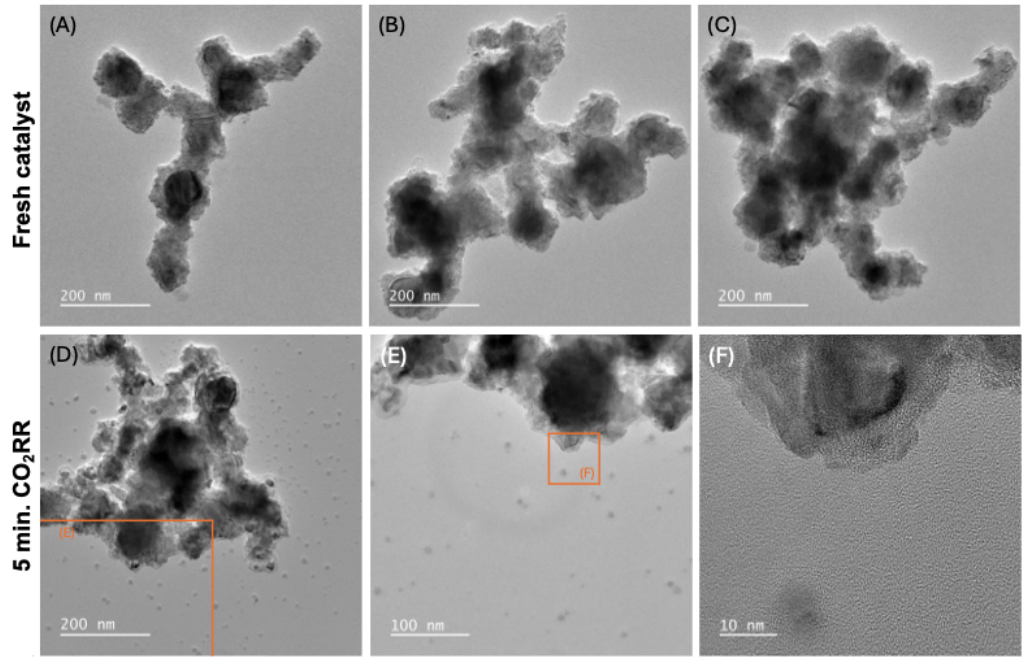

Figure 2 Near identical location TEM results. (A), (B) and (C) show representative images of fresh catalyst, (D) shows copper nanoparticles after 5 min of CO_2RR. Newly formed small particles are visible around the copper catalyst. (E) provides a close-up view of region marked in (D) at the edge of the original copper particle and newly formed particles. In (F) lattice is visible for both the original copper particle and the newly formed particles.

No morphological changes were observed when no electrical potential was applied (Figure S38a), suggesting that the alterations in morphology occurred solely under electrical bias and were not a result of merely immersing the copper-coated cathode in the electrolyte. EDS analysis also confirmed that the smaller nanoparticles formed belongs to copper and not an impurity (Figure S38b-c).

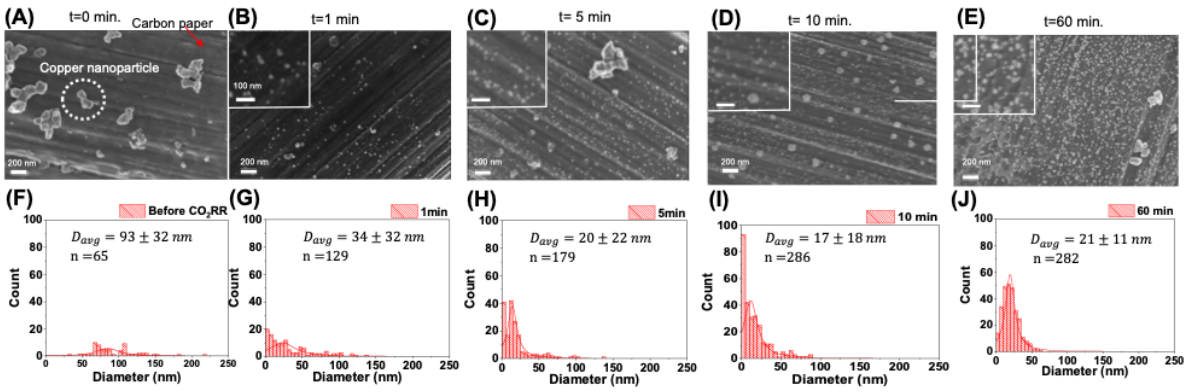

Figure 3 (A-E) Secondary electron (SE) contrast scanning electron microscopy (SEM) images of copper nanoparticles at different reaction times (t) from 0 to 60 minutes. Insets are showing a zoomed subset of the image showing the density of smaller copper particles increased over time. (F-J) Particle size distribution based on SEM image analysis. The mean particle diameter (D_{avg}) is given in (F) to (J) as well as the number of counted particles (n). Scale shown in (A) is the same for all images.

It is possible that the morphological changes of the copper nanoparticles observed under the SEM was affected by oxidation caused by post-air and electrolyte exposure since copper is easily oxidized by air and liquid. To test whether this is the case, we monitored the morphological changes under in situ conditions by using electrochemical atomic force microscopy (EC-AFM), depicted in Figure 4. In EC-AFM, the similar general trend was observed: the initial mean particle size of the copper nanoparticles before CO_2RR was ~139 nm, the median particle size 137 nm, with minimum particle size of 93 nm and maximum particle size of 206 nm. After 3 minutes of CO_2RR, the mean and median particle size dropped to 68 nm with minimum particle size being 61 nm and the maximum particle size 73 nm. After 30 minutes of CO_2RR, the mean particle size is 52 nm, the median particle size 54 nm, the minimum particle size 28 nm and the maximum 73 nm. The in situ electrochemical AFM measurements confirm that the formation of the small

copper nanoparticles during the initial stage of reaction is the result of CO_2RR. The resulting current data from EC-AFM is provided in supporting information (Figure S39) and a table of all particle sizes is given (Table S4).

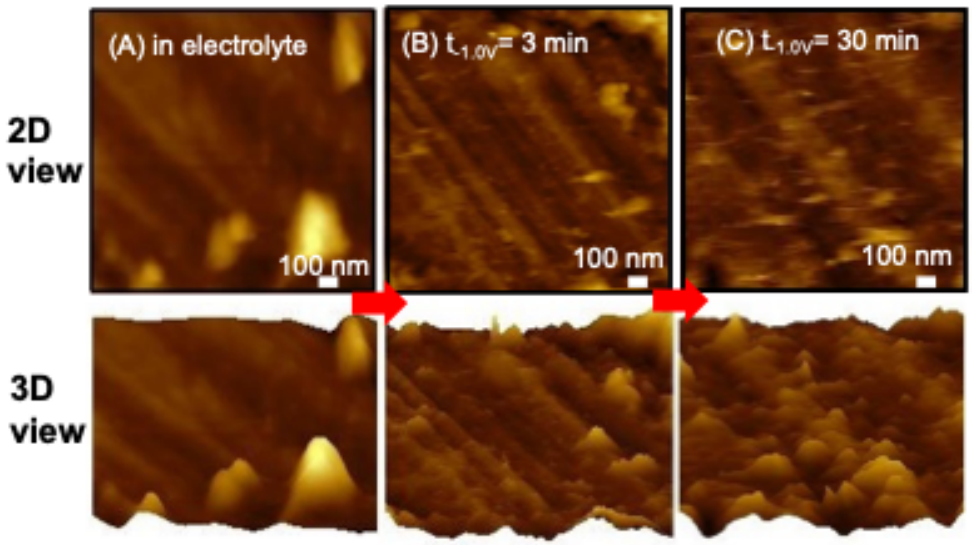

Figure 4 (A) EC-AFM Height retrace images of copper nanoparticles on carbon paper (A) in 0.1 M $KHCO_3$ solution before CO_2RR, (B-C) after CO_2RR for 3 and 30 minutes. The bottom row is the 3D view.

XRD analysis of copper catalyst after CO_2RR (Figure 5A) showed reconstruction of the copper nanoparticles during the reaction as evident in the variation of the normalized intensity for different facets vs. reaction time (Figure 5B). Two high-index facets (220) and (311) disappear during the early stage of the reaction. High-index facets usually have an open surface structure featuring a high density of atomic steps, kinks and lower-coordination atoms.[30, 31] These surface defects can lead to a change in adsorption energy for intermediates onto the surface of the catalyst.[32] The (311) high-index surface was previously determined to have a higher propensity to produce C_{2+} products.[33] It is likely that the higher reactivity of the (311) surface with higher reactivity underwent reaction and reconstruction during the initial CO_2RR stage, such as dissolution of surface copper species as shown in later ICP-OES analysis.

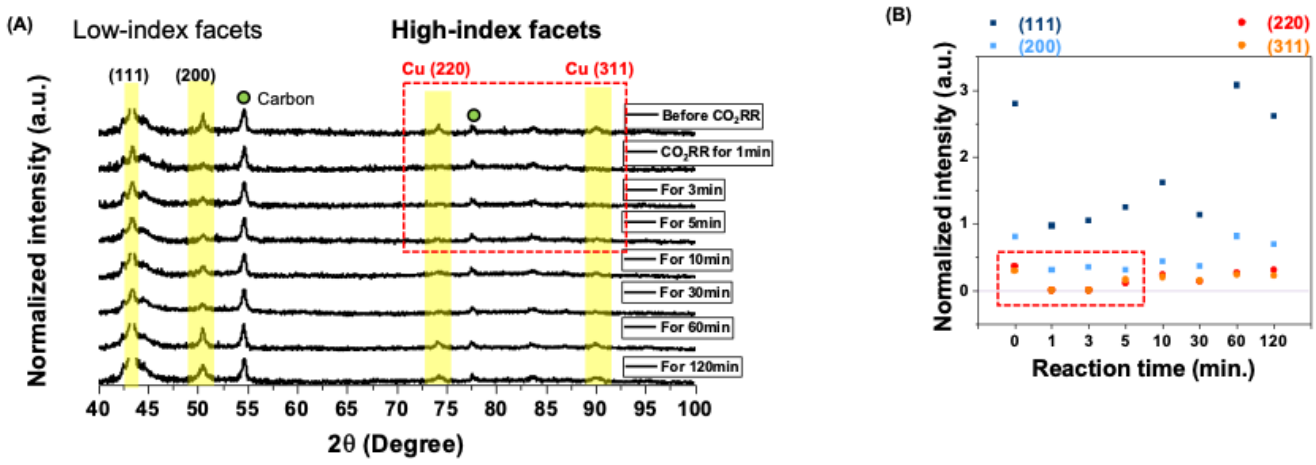

182

183 **Figure 5 Ex-situ XRD analysis of copper catalyst at different CO_2RR reaction times. (A) XRD**
184 **diffractogram and (B) normalized intensity of different copper facets.**

185 **2. Product Evolution During CO_2RR**

186 To understand how the smaller nanoparticles were formed and to correlate the morphological
187 changes with CO_2RR reaction products, the evolution of products was studied with gas
188 chromatography (GC) and ^1H nuclear magnetic resonance (NMR). The current density increased
189 slightly as the smaller nanoparticles formed until 40-60 minutes of reaction time had elapsed, and
190 then the current density decreased marginally as the mean copper nanoparticle size increased by
191 aggregation (Figure 6A). During the reaction, three gaseous products (hydrogen (H_2), carbon
192 monoxide (CO), methane (CH_4)], and one liquid product (formate ($HCOO^-$)) were produced
193 (Figure 6C). However, their selectivity changed differently over time. The Faradaic efficiency (FE)
194 of hydrogen production gradually increased whereas that of methane and carbon monoxide
195 persistently decreased. Formate was temporarily produced coinciding with the occurrence of
196 smaller nanoparticles until 60 minutes (Figure 6C-D). Formate concentrations in solution were
197 observed between 0.08 mM (minimum) to 3.3 mM (maximum). It appears that formate production
198 is inversely related to the copper particle size (Figure 6B-D) while other carbon products decrease
199 continuously with reaction time (Figure 6C), at least qualitatively. There are several possibilities
200 that can explain the temporary formate production. First, the reduction of oxidized copper to the
201 zero-valence state could influence formate production in two possible ways: one is that only
202 reduced copper produces formate, from which it would be expected that the formate production is

stable, which is not what we observe, nor has it been reported in any other studies to our knowledge. Second, the reduction of copper oxide could also take a certain amount of time (supported by in situ XAS result presented in a later section) and a mixed copper/copper oxide phase could favor formate production due to the transient presence of copper oxide, which could explain the temporary production of formate. This matches with previous studies showing the CuO favors formate production[34]. A third possibility is that smaller copper particles favor formate production. Previous studies observed that nanoporous polycrystalline copper favored formate production at sizes smaller than 22 nm.[35] Similar observations were made for dendritic Cu catalysts.[36]

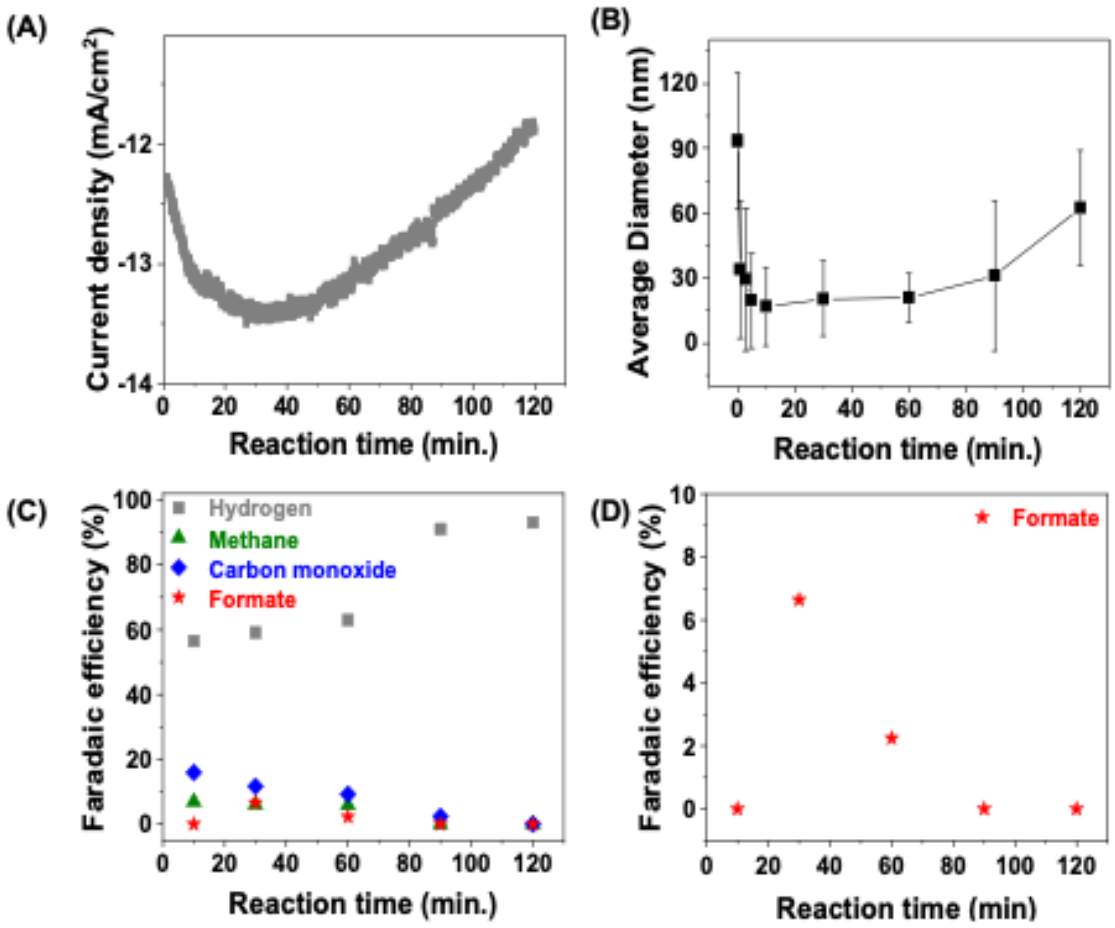

Figure 6 (A) Total current density. (B) Mean diameter (D_{avg}) of copper as a function of reaction time as determined by SEM image analysis. (C) Faradaic efficiency (FE) of hydrogen, methane, carbon

monoxide, and formate as a function of time. (D) FE of formate. Formate was temporarily produced until 40 minutes of CO_2RR.

3. Control Experiments to Identify Possible Effect of Intermediates

Different reaction intermediates are proposed in the literature to cause copper degradation during CO_2RR[37]. One pathway described is that the degradation of copper into smaller nanoparticles leads to the formation of isolated low-coordinated sites which favors hydrogen evolution reaction (HER) over CO_2RR.[38] Another pathway is CO intermediate adsorption[37]. Based on our experimental results and analysis, we propose ligand-assisted dissolution as a possible degradation mechanism where the ligand is the observed CO_2RR product, formate in this case. This type of ligand-assisted dissolution (also commonly termed "ligand-promoted" or "ligand-induced") is a commonly observed phenomenon in geochemistry[39, 40], e.g., in the case of oxalate enhancing the dissolution of Al_2O_3[41] or salicylate enhancing gibbsite dissolution[42]. Recently, it has been studied for metal dissolution[43] and also has been proposed to explain copper electrocatalyst degradation in the presence of amines[44]. Other ligands, e.g., humic acid, also have been shown to promote copper dissolution[45].

To test our hypothesized role of formate species, we conducted three different control experiments to identify which intermediate is causing the particle size changes: *(1) hydrogen evolution reaction control experiment (HER), (2) electrochemical CO reduction control experiment (CORR), (3) formate added to CORR control experiment (CORR with formate) and (4) SO_2 blocked formate adsorption control experiment (CO_2RR with SO_2).*

Since the dominant reaction is HER as evidenced by high FE of H_2 (Figure 6C), we first tested HER. In this first control experiment called *hydrogen evolution reaction control experiment*, only argon gas was supplied to test whether hydrogen gas evolution and binding to copper catalyst causes copper nanoparticle morphology changes. SEM image analysis did not show any reduction in particle size as a function of reaction time (Figure S4). Since the pH of the *hydrogen evolution reaction control experiment* is lower than the CO_2RR experiment, we also performed control experiments in which we adjusted the pH to match the pH during CO_2RR (pH = 6.8). Particle size

changes were much slower than during the CO_2RR, with a reduction of particle size only visible after 60 min of reaction (Figure S40 + S41).

Second, CORR was tested since previous studies have reported that CO is a crucial intermediate. Early work found that the reduction of CO yields very similar product distribution as CO_2RR on copper, highlighting that CO is a key intermediate[46, 47]. In the second control experiment, called *CO reduction reaction control experiment*, CO was supplied instead of CO_2, to identify whether the CO intermediate causes Cu size changes.[48] The size change occurs at a much slower pace in this *control* experiment than CO_2RR as compared in Figure S42. Clearly, significant morphological changes of the Cu catalyst only occur under CO_2RR. The main difference in products between the HER/CO control experiments and the CO_2RR is that formate was temporarily produced during CO_2RR, suggesting a major effect of formate in causing copper size changes.

Therefore, we tested our hypothesis that ligand-assisted dissolution is causing copper particle size changes with a third control experiment called *added formate CO reduction reaction control experiment*. In this CORR experiment, we intentionally added a controlled concentration (1 mM and 4 mM) of potassium formate, which was chosen to match formate concentration observed in CO_2RR experiments. Smaller copper nanoparticles quickly (within 10 min) formed after adding 4 mM of potassium formate in the electrolyte even under CO supply condition (Figure 7A-F) and the observed size distribution matched well with the one produced during CO_2RR (Figure 7A-F). Results for 1 mM formate are given in Figure S43. We therefore conclude that the significant morphological change of copper particles is mostly caused by formate during CO_2RR.

The findings suggest that copper dissolution during CO_2RR is specifically induced by the combined presence of formate and an applied cathodic potential. Importantly, this mechanism is fundamentally distinct from classical oxidative corrosion. While cathodic conditions typically suppress metal dissolution, strong ligands such as formate can directly complex with copper even under reducing conditions. Studies have shown that the formation constants for copper-ligand complexes[25] particularly with chelating or π-acceptor ligands like amines[49], acetate and formate[25, 50] are sufficiently high to render the overall free energy change for dissolution favorable, provided

that the chemical stabilization by the ligand offsets the unfavorable redox potential. This ligand-induced dissolution does not require an external oxidant and is driven by direct complexation, not by potential-driven oxidation. Also, interfacial availability of formate at copper-based cathodic active sites may boosts this complexation.

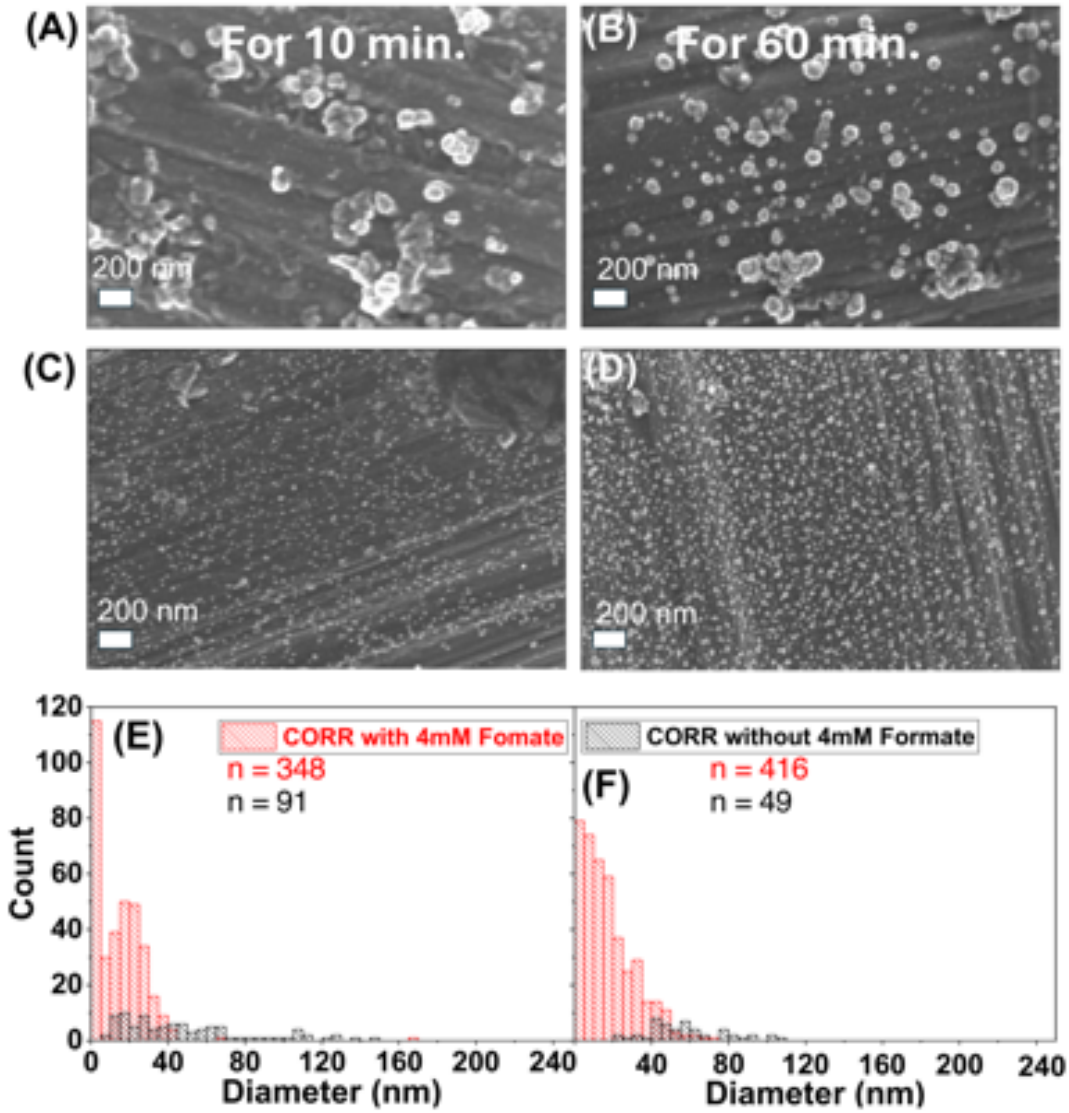

Figure 7 Particle size analysis of control experiments. SE contrast SEM images after (A) *CO reduction reaction control experiment* for 10 minutes and (B) 60 minutes. (C) *Added formate CO reduction reaction control experiment* for 10 minutes and (D) 60 minutes. (E) Particle size distribution based on SEM image analysis of the two control experiments for 10 minutes and (F)for 60 minutes.

To test whether copper still changes its size once formate adsorption is blocked, we conducted SO_2 blocked formate adsorption control experiment in which we added SO_2 during CO_2RR reaction. Particle size analysis of SEM images (Figure 8A+B) showed that after 10 min of CO_2RR in presence of 200 ppm SO_2, the average particle size only slightly decreased, to 50 ± 35 nm. After 60 min of reaction, the average particle size was still 56 ± 42 nm. Product distribution also changed in the presence of SO_2. Without SO_2, the FE of formate was 0 after 10 minutes, 6.64% after 30 minutes and 2.23% after 60 minutes (Figure 8D). In the presence of SO_2, no formate was produced after 10 and 30 minutes, and FE was 5.48% after 60 minutes (Figure 8B). This control experiment shows that when SO_2 is present, formate is formed later, and the copper particle size does not significantly change within the first hour of reaction. One possible explanation for the later onset of formate formation could be that its production is sensitive to the oxidation state. It can be expected that the presence of SO_2 will affect the oxidation state of Cu.

The observed suppression in formate production is attributed to the strong adsorption of SO_2 on copper surfaces[51], which occurs preferentially at the same active sites responsible for CO_2 adsorption and activation. Although the precise atomic configuration of these active sites under aqueous electrochemical CO_2RR remains elusive, surface science and theoretical studies consistently indicate that SO_2 exhibits markedly stronger binding to copper than CO_2 or its reduction intermediates[52-54]. Density functional theory (DFT) calculations further confirm the higher adsorption energies of SO_2 relative to CO_2, which explains the competitive displacement of CO_2 and consequent inhibition of formate[55]. These findings agree with electrochemical observations (Figure 8C) that SO_2 acts as a catalyst poison by occupying crucial copper sites, thus reducing the available active area for CO_2 reduction to formate. While in-situ identification of the SO_2 adsorption site under reaction conditions is still not available due to experimental challenges, the collective evidence supports the conclusion that SO_2 hinders formate production primarily through direct site competition and surface modification mechanisms.

Apart from the above control experiments, because previous studies[56] observed the appearance of Cu 2S peaks in XPS analysis, we tested our samples using XPS, however we were not able to observe this peak. We observed SO_3^{2-} peaks (Figure 8E). This peak could either be due to strong interaction of copper with SO_2 or due to SO_2 oxidation in the electrolyte or interaction with surface

oxygen. Due to the applied reductive potential, SO_2 oxidation in the electrolyte is unlikely.[57] Since the SO_2 blocked formate adsorption control experiment did not show any formate production and no significant reduction in particle size, this further indicates that formate is accelerating the copper dissolution via a ligand-assisted dissolution mechanism.

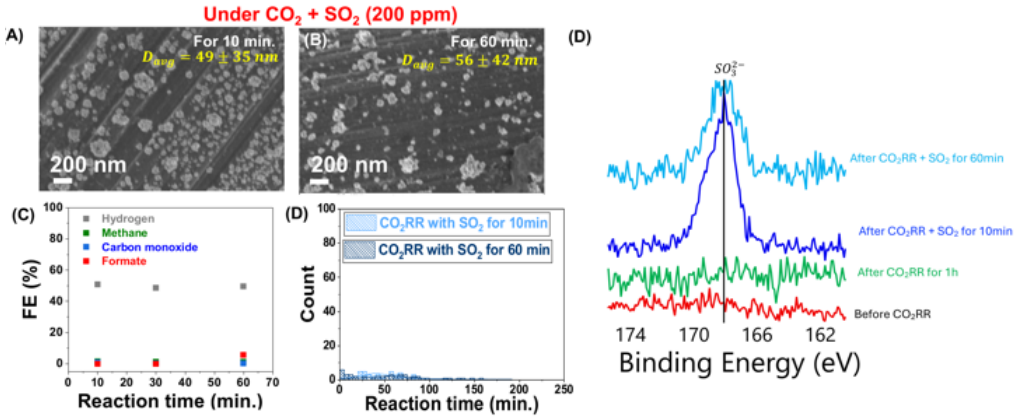

Figure 8 Effect of SO_2 on CO_2RR. SEM images of electrode after 10 min (A) and 60 min (B) CO_2RR in presence of 200 ppm SO_2. (C) Faraday efficiency of rection products as function of reaction time. (D) Particle size distribution of images shown in (A) and (B). (E) XPS data showing SO_2 binding.

4. Analysis of the Dissolution of Copper Nanoparticles in the Electrolyte to Identify Reaction Mechanism

Due to the overestimation of particle size in the SEM analysis, it is not possible to distinguish based on SEM analysis whether the particle size reduction is due to the formation of smaller copper nanoparticles via a dissolution/reprecipitation mechanism or due to breaking up of agglomerates. One possible indication for the dissolution/reprecipitation mechanism would be the release of copper ions into the electrolyte solution.

To test whether copper is dissolved into the electrolyte, we analyzed the copper concentration in the electrolyte using inductively coupled plasma optical emission spectroscopy (ICP-OES) at different stages of CO2RR as well as control experiments. As shown in Figure 9, we observed that ~10% of the total copper was dissolved (equivalent to 4.5 ppm copper detected in the solution) into the electrolyte even after 1 min of CO2RR. The dissolved copper concentration decreased

exponentially, with 1.8 ppm after 10-minute reaction, 1.0 ppm after 30-minute reaction and 0.76 ppm after 1 hour reaction. In contrast, the hydrogen evolution reaction control experiment showed much lower copper concentration (0.7 ppm after 1-minute reaction, 0.7 ppm after 10-minute reaction, 0.6 ppm after 30-minute reaction and 0.4 ppm after 1 hour reaction), indicating that HER does not lead to significant copper dissolution. Similar trends were observed in control experiments for CORR and CO2RR with SO2, which yielded negligible copper dissolution over the 60-minute observation period. This further supports our hypothesis regarding the interaction between formate and the copper catalyst under electrochemical potential, suggesting that formate induces both the dissolution and reprecipitation of the copper electrocatalyst during CO_2RR. A table with ICP-OES measurement data is given in the supporting information (Table S5).

The temporal discrepancy between the observation of formate using NMR (Figure 8D), where more formate is present after 60 minutes compared to 10 minutes and the aqueous copper concentration (Figure 9), where the copper concentration is higher after 10 minutes compared to 60 minutes, can be possible explained by the following reasoning: (1) unidentified complexation of formate by copper or potassium and (2) changes in reactive sites on copper particles due to dissolution and reprecipitation. The focus of our NMR measurements is the quantification of formate, which proton NMR with water suppression and DMSO as internal standard is a suitable method for[58] and not the dynamics of formate complex formation in the solution. It can therefore be possible that there is formate present in solution either as potassium formate or copper formate complex. Additionally, previous studies have shown that different crystal morphologies[32] or defects[59] stabilize reaction intermediates differently. It can therefore be expected that due to the dissolution and reprecipitation of the copper catalyst, the reactive sites on the copper particles are modified.

Based on the particle sizes analysis derived from SEM image of the control experiments which is indeed qualitative and ICP-OES results which is quantitative, we can conclude that the dissolution of copper during CO_2RR relative to HER, CORR, CO_2RR with SO_2 is due to the presence of formate as well as applied electrochemical potential and the dissolved copper ion were redeposited in the form of smaller nanoparticles under the cathodic potential only during CO_2RR.

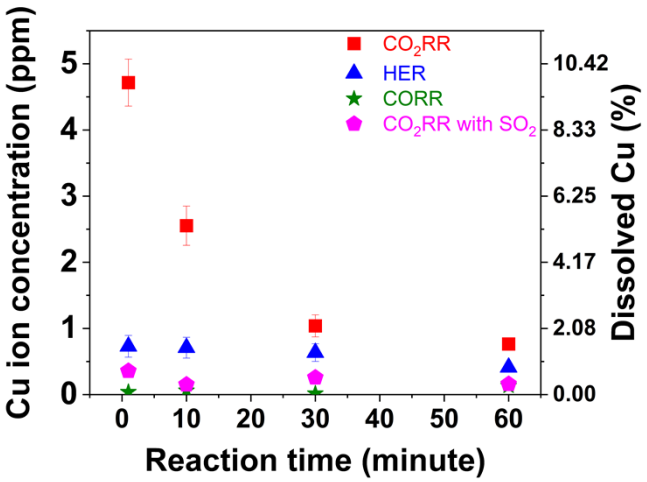

Figure 9 Electrolyte copper concentration measured by inductively coupled plasma optical emission spectroscopy (ICP-OES) of electrolyte from CO_2RR, HER, CORR and CO_2RR with SO_2 reactions at different reaction times.

5. In-situ XAS

To monitor the structural evolution of copper in situ and further test our hypothesis that formate enhances copper dissolution, we collected Cu K edge XAS spectra in an in-situ electrochemistry setup (Figure S44). Three different experiments were conducted, (1) CO_2RR, (2) *HER control* experiment and (3) *added formate hydrogen evolution reduction (formate-HER) reaction control experiment.* As shown in Figure 10, before the reaction, oxidized copper can be detected. Under all reaction conditions, with the increase of the reaction time, the concentration of oxidized copper gradually decreased and that of metallic copper gradually increased. After ~20 minutes reaction, most of the copper is present in reduced form. After ~110 minutes, more than 90% of the copper are present in reduced state.

To compare the reduction rate of copper under the three different experimental conditions, linear combination fitting was performed. The fitting energy range is 8970 to 9030 eV. For the fitting, the two standards are the spectra collected before the reaction and the last scan collected at 160 min of reaction. As shown in Figure 10D, the reduction rate of copper follows the trend of *formate-HER>HER>CO_2RR* with *HER/CO_2RR* being very similar. By performing EXAFS analysis, it was found that after 160 min reaction, the Cu-Cu coordination number in the obtained Cu metallic

species is ~10 (Table 1), smaller than 12, suggesting that nanosized Cu dominates for all studied reactions.

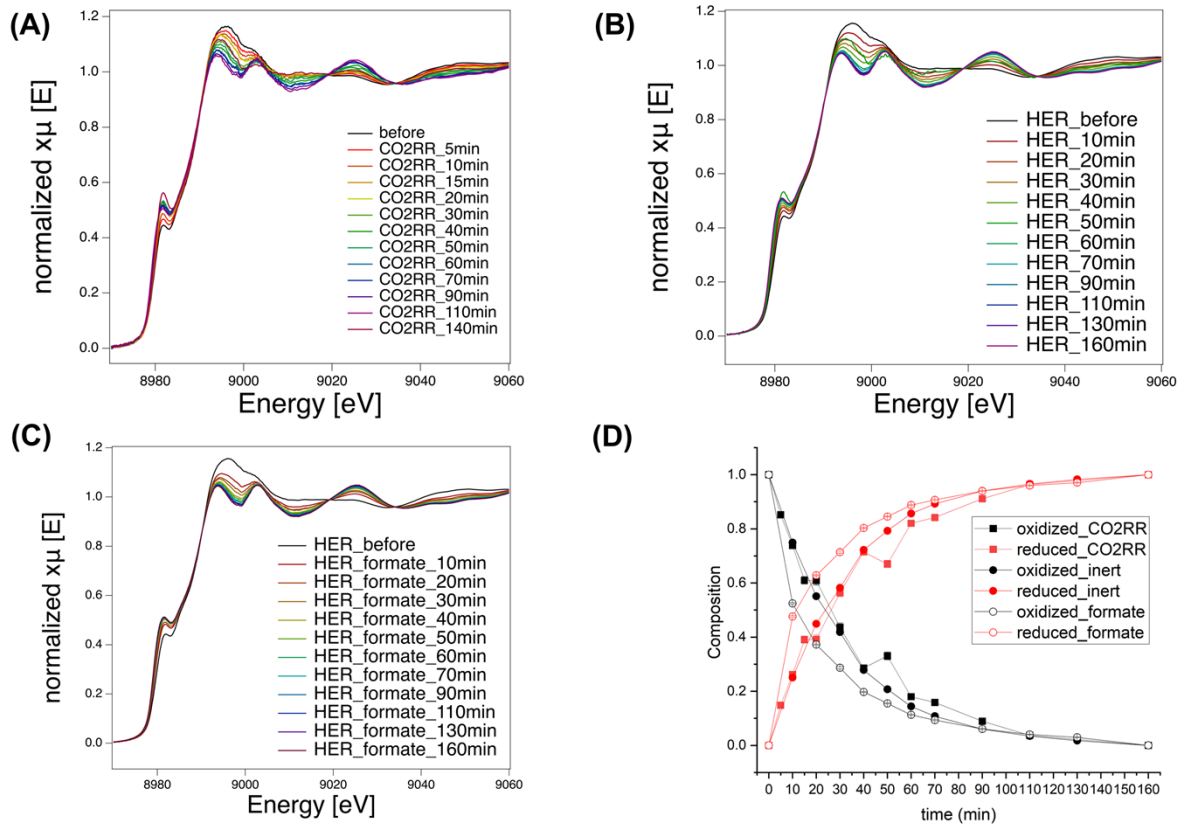

Figure 10 In situ XAS results. Bias induced time-dependent change of Cu K-edge XANES spectra under (A) *CO_2RR*, (B) *HER*, (C) *formate-HER*. (D) The time-dependent change of copper composition (oxidized/reduced) in *CO_2RR*, *HER*, and *formate-HER* experiments.

Table 1 The best fitting results obtained for the catalyst being exposed to CO_2RR for 160 min. The fitting k range is 2 - 11 $Å^{-1}$ and R range is 1 - 2.8 Å. The amplitude reduction factor (0.92) was obtained by fitting the spectrum of copper foil. Table provides N (coordination number), R (distance) (Å), σ^2 (variance) ($Å^2$) and ΔE (energy shift) (eV).

Sample	Path	N	R (Å)	σ^2 ($Å^2$)	ΔE (eV)
Copper foil	Cu-Cu	12	2.544±0.002	0.0087±0.0003	3.5±0.4

Before	Cu-O	1.4±0.2	1.90±0.01	0.004±0.002	10±1
	Cu-Cu	4.8±0.4	2.542±0.002	0.0075±0.0006	5.1±0.7
HER_60min	Cu-Cu	9.2±0.5	2.540±0.002	0.0078±0.0005	4.2±0.2
HER_70min	Cu-Cu	9.3±0.6	2.539±0.002	0.0079±0.0005	4.2±0.2
HER_90min	Cu-Cu	9.4±0.5	2.540±0.002	0.0077±0.0005	4.2±0.2
HER_110min	Cu-Cu	9.7±0.6	2.539±0.002	0.0077±0.0005	4.2±0.2
HER_130min	Cu-Cu	9.7±0.5	2.540±0.002	0.0079±0.0004	4.2±0.2
HER_160min	Cu-Cu	9.7±0.4	2.540±0.002	0.0077±0.0004	4.2±0.2
Formate-HER-60min	Cu-Cu	9.2±0.7	2.543±0.002	0.0080±0.0006	4.7±0.2
Formate-HER-70min	Cu-Cu	9.7±0.6	2.544±0.002	0.0083±0.0006	4.7±0.2
Formate-HER-90min	Cu-Cu	9.6±0.6	2.543±0.002	0.0081±0.0005	4.7±0.2
Formate-HER-110min	Cu-Cu	9.8±0.5	2.543±0.002	0.0081±0.0004	4.7±0.2
Formate-HER-130min	Cu-Cu	9.9±0.7	2.543±0.002	0.0081±0.0006	4.7±0.2
Formate-HER-160min	Cu-Cu	10.0±0.5	2.543±0.002	0.0081±0.0005	4.7±0.2
CO_2RR_60min	Cu-Cu	8.7±1.0	2.543±0.004	0.008±0.001	4.8±0.4

CO_2RR_70min	Cu-Cu	8.2±0.8	2.543±0.003	0.0073±0.0008	4.8±0.4
CO_2RR_90min	Cu-Cu	9.0±0.8	2.543±0.003	0.0078±0.0007	4.8±0.4
CO_2RR_110min	Cu-Cu	10.3±1.0	2.543±0.004	0.00791±0.0009	4.8±0.4
CO_2RR_160min	Cu-Cu	10.0±0.9	2.541±0.003	0.0086±0.0008	4.8±0.4

6. Comparison of In Situ XAS Results and H-Cell Results

When we compare the particle size changes measured by SEM/TEM and AFM analysis with in situ XAS results, we observe contrasting qualitative results: results based on SEM/TEM and AFM analysis show that the copper particle size decreases from larger particles (~30-90 nm) to single digit nanometer size particles. XAS results show that the copper particle size is in the nanoparticle size regime from the start of the experiment and does not significantly change, which is evident from the coordination number of copper being close to 10 and not changing over the experiments. One possibility that reconciles these seemingly contradicting results is that the copper particles form agglomerates of oxidized particles due to oxidation during sample preparation. The particle size observed in SEM, TEM and AFM therefore presents the agglomerate particle size. These agglomerates break up during CO_2RR. The copper release into solution measured by ICP-OES could be explained if we assume a shell of copper oxide forming around the reduced copper particles, holding the agglomerates together, which then dissolved along boundaries between particles. This would explain both why we are seeing oxidized particles being present in XAS analysis, as well as different particle sizes observed in SEM/TEM/AFM compared with XAS.

Another potential difference between in situ XAS result and the lab electrocatalysis CO_2RR result is the kinetics of the reduction of oxidized Cu to metallic Cu during CO_2RR. The oxidation state of Cu could impact the dissolution rate of Cu during the reaction, which seems fast (less than 10 min) according to the formate production trend, the SEM/AFM analysis of Cu size and the ICP analysis of dissolved Cu species. This contrasts with the in situ XAS result showing a rather slow

reduction rate. For example, about half of the copper is still in oxidized form for the first 20 minutes of reaction. Such a discrepancy in Cu oxidation state could be due to the difference in the design of the electrochemical cell between in situ XAS study and the rest experiments. The XAS electrochemical cell is a flow-through cell, whereas the rest of experiments used the H-cell configuration. It can therefore be assumed that the reduction of copper in the H-cell is faster than 20 minutes, but we cannot state that with certainty since we do not have any data on copper oxidation state during the reaction.

Conclusion

Morphological evolution of copper nanoparticles was investigated by combining in- and ex-situ characterization to ascertain which intermediate is affecting the structural and morphological change of the copper nanoparticles during CO_2RR. We controlled gas (Ar, CO, and CO_2) and liquid (with/without formate) conditions. We find that the morphology as well as dissolution of the copper nanoparticles in the electrolyte during electrical bias was significantly changed by formate whereas *H and *CO did not significantly affect morphology and dissolution of the copper nanoparticles. Our results indicate that the strong binding of formate with copper nanoparticles causes ligand-assisted dissolution which drives the morphological and structural change of Cu nanoparticles under CO_2RR.

Experimental Section

7. Preparation of catalyst

Copper nanoparticles were purchased from US research. 0.8 mg of catalyst was dispersed in a mixture of 1.25 mL IPA (Isopropyl alcohol) and 7 μL of ionomer (XA-9 Alkaline Ionomer 5% in ethanol, Dioxide Materials). The mixture was sonicated for at least 20 minutes to produce the copper nanoparticle ink and then the spray-casted on a carbon paper (Sigracet 39AA, Fuel Cell store). For the anode preparation, IrO_2 powder (99%, IrO_2 powder, ThermoScientific) was affixed on a titanium mesh. 24 mg of the IrO_2 were mixed with IPA and 12.5 μL nafion (D520, Ion Power). The mixture was sonicated for 20 minutes and then spray-casted on the titanium screen (Platinized

Titanium screen, Fuel Cell store). SEM imaging of the Cu catalyst showed multiple facets (Fig. S1).

8. Electrochemical experiments

Electrochemical measurements were carried out with an H-Type electrochemical cell and SP-200 potentiostat (BioLogic). All potentials were measured in volts against an Ag/AgCl reference electrode (filled with 4 M KCl) and converted to the RHE reference scale using:

$$E\ (\text{vs RHE}) = E\ (\text{vs Ag/AgCl}) + 0.199 + 0.0591 \times pH, \quad (1)$$

where E (vs. RHE) represents the potential (V) of the reversible hydrogen electrode (RHE), E (vs Ag/AgCl) represents the experimentally measured potential (V) against the Ag/AgCl reference, and pH is the pH of the electrolyte (pH 7). The cathode and anode were separated by anion exchange membrane (X37-50, Dioxide Materials). Electrolyte solution was 0.1 M $KHCO_3$ solution, which was prepared from 99.7% purity (237205-500G, Sigma Aldrich) salt with deionized water (18 mΩ·cm). CO_2 gas was bubbled through the electrolyte to prepare CO_2-saturated electrolyte for at least 30 minutes before starting the experiment. Then, CO_2 was constantly bubbled with a flow rate of 10 mL/min through the electrolyte to prevent depletion of CO_2 in the electrolyte and allow continuous analysis of gaseous products via a gas chromatograph. For all electrochemical experiments, the experiments were started immediately after setup, and no open circuit potential measurements were performed. Previous studies[23] have shown that the duration of open circuit potential measurements can affect the copper degradation and we therefore controlled for this variable. For hydrogen evolution reaction and carbon monoxide reduction reaction control experiments, either Ar or CO gas (flow rate 10 mL/min) was supplied to the cell after bubbling Ar or CO in the electrolyte for at least 30 minutes. Before conducting the control hydrogen evolution reaction, a small volume of hydrochloric acid (50 μL) was added to the electrolyte to lower the pH of the electrolyte to match the pH of CO_2 reduction condition. For the potassium formate-added control experiment, 1 mM and 4 mM of potassium formate (BioUltra, >99.0%, Sigma Aldrich) was added to 0.1 M $KHCO_3$ and measured with NMR to confirm the formate peak.

In the SO_2 contaminant study, 10 mL/min of SO_2/Ar (200 ppm SO_2 balanced Ar, Airgas) gas was bubbled through the electrolyte for at least two hours and then mixed with 10 mL/min of CO_2 gas to initiate the CO_2RR reaction. pH measurements were conducted with Denver Instrument, Model 250 using a three-point calibration.

9. Liquid and gas products analysis

545 μL of the reacted electrolyte was mixed with 50 μL of D_2O (Sigma Aldrich) and 5 μL of dimethyl sulfoxide (DMSO, 10 mM as an internal standard, >99.7%, Fisher)] for NMR (400 MHz NMR Spectrometer) measurements. The one-dimensional H spectrum was measured under water suppression mode. Figure S9 shows the NMR spectra of formate and Figure S10 gives the raw data. The Faradaic efficiency (FE) of liquid products was calculated as follows. First, the molar concentration of each liquid product (C_x) was calculated using the following formula:

$$C_x = \frac{I_{liquid}}{I_{DMSO}} \times \frac{N_{DMSO}}{N_{liquid}} \times C_{DMSO}, \quad (2)$$

where I, N, and C are the integral area of the NMR signal, the number of protons, and the concentration of the compound of interest (liquid product x) or the calibrant (DMSO), respectively. Then, the FE of liquid products was calculated using the following formula:

$$\mathrm{FE} = \frac{q_1}{q_{tot}} = \mathrm{f} \times c_x \times V \times z_1 / q_{tot} \times 100, \quad (3)$$

where q_1, f, V, z_1, q_{tot} are the charge consumed for generation of a particular liquid product, the faraday constant (C/mol), the volume of the reacted electrolyte (liters), the number of electrons to produce the liquid product, and the total charge ($q_{tot} = \int Idt$), respectively. The amount for each gaseous product, G_x, was quantified by gas chromatography (GC) equipped with both flame ionization detector (FID) and thermal conductivity detector (TCD) (SRI 8160C). The FE of the gas products were determined via the following formula:

$$\mathrm{FE} = \frac{q_1\,(output)}{q_{tot}\,(input)} = \mathrm{f} \times G_x \times z_g / q_{tot} \times 100, \quad (4)$$

where G_x is the amount of gas product in moles produced during a target reaction section, z_g is the number of electrons to produce a gas product, and q_{tot} is the total charge determined by the integration of current during the target reaction time session ($\int Idt$).

10. Catalyst characterization

The morphology of the samples was analyzed using scanning electron microscopy (SEM, MERLIN SEM, Zeiss) at 1 kV, transmission electron microscopy (TEM) at 300 kV using a FEI Titan TEM, and electrochemical atomic force microscopy (EC-AFM, MFD-3D). The tip was PNP-TR-50. For EC-AFM, the leakless Ag/AgCl reference was used with customized titanium plate as an anode. The bias and current data were collected by using a SP-200 potentiostat. The compositions of the samples were studied using energy-dispersive X-ray spectroscopy (EDS) system (MERLIN SEM, Zeiss) coupled to the SEM. X-ray diffraction (XRD) patterns were collected using an PANalytical X-ray Diffractometer with a CuKα X-ray source (λ = 1.540598 Å), soller slit (0.04 rad), and 0.026 steps. The peaks were analyzed with single/multi gauss fits from Origin 2018 version software.

11. ICP-OES

Copper concentration in the electrolyte were analyzed using a ThermoFisher Scientific iCAP 7400 inductively coupled plasma - optical emission spectrometer (ICP-OES). 2% nitric acid for dilution was prepared by mixing deionized water purified with a MilliQ system (Millipore) and Ultrapure II nitric acid (J.T. Baker). Solutions were filtered with 0.22 μm syringe filters and then 1:10 dilutions of solutions were prepared in 2% HNO_3. Copper emissions were measured in radial mode at 324.754 and 327.396 nm. Internal standard was 5 ppm yttrium. A commercial elemental standard for copper (High Purity Standards, Charleston, South Carolina, USA) was used to prepare a 50 ppm stock solution. Intelligent dilution by the automatic sample loader (Elemental Scientific, Omaha, Nebraska) was used to generate a seven-point standard curve with concentrations of 0.5, 1, 2, 5, 10, 20, and 50 ppm.

12. XPS

X-ray photoelectron spectroscopy (XPS) was performed using a Thermo Scientific (Waltham, MA, USA) Model K-Alpha XPS instrument. The instrument utilizes monochromated, micro-focused, Al K_α X-rays (1486.6 eV) with a variable spot size (i.e., 30-400 μm). Analyses of the sample was performed with the 400 μm X-ray spot size for maximum signal and to obtain an average surface composition over the largest possible area. The instrument has a hemispherical electron energy analyzer equipped with a 128-channel detector system. Base pressure in the analysis chamber is typically 2×10^{-9} mbar or lower. Samples were prepared for analysis by attaching the samples directly to the XPS holder using metal clips. Survey spectra (pass energy = 200 eV) were acquired for qualitative and quantitative analysis and high-resolution core level spectra (pass energy = 50 eV) were acquired for detailed chemical state analysis. All spectra were acquired with the charge neutralization flood gun turned on to maintain a stable analysis condition. The flood gun uses a combination of low energy electrons and argon ions for optimum charge compensation. The typical pressure in the analysis chamber with the flood gun operating is 2×10^{-7} mbar.

13. In situ X-ray absorption spectroscopy (XAS)

In situ Cu K edge XAS data were collected at the QAS beamline (7-BM) of National Synchrotron Light Source II (NSLS II), Brookhaven National Laboratory. All data were collected in fluorescence mode. A three-electrode arrangement (the same setup as those described in electrochemical measurements) was used for the in situ measurements. The measurements were performed in a half-cell of a commercial in situ electrochemical cell (GDE XRD EC 1.75 ml, MSE Supplies) with a Kapton tape window, allowing X-ray transmission. A picture of the setup is given in Figure S8. Electrolyte preparation was the same as for H-type cell experiment. 0.8 mg of copper was dispersed in a mixture of 1.25 mL IPA (Isopropyl alcohol) and 7 μL of ionomer (XA-9 Alkaline Ionomer 5% in ethanol, Dioxide Materials). The mixture was sonicated for at least 30 minutes to produce the copper nanoparticle ink and then spray-casted on a carbon paper (30% hydrophobicity). Current data was monitored using a SP-300 potentiostat. The electrolyte was circulated using a peristaltic pump at 10 mL/h. Three different experimental conditions were

tested: 1) CO_2RR, 2) HER 3) HER with added formate. For HER, Ar gas was bubbled through the electrolyte for 1 hour. For HER with added formate, 4 mM potassium formate (BioUltra, >99.0%, Sigma Aldrich) were added into the electrolyte before bubbling the electrolyte with Ar gas for 1 hour. XAS data were processed and analyzed by using the IFEFFIT package[60].

14. Near Identical Location TEM

Near Identical location TEM was performed using PELCO Pinpointer Grids. Fresh copper catalyst was mixed with isopropanol, sonicated for 30 minutes and then drop casted onto the grid. A FEI Titan instrument was used at 300 kV to collect TEM images before electrochemical experiments. Electrochemical experiments were conducted in the H-cell setup described previously. After 5 minutes of CO_2RR, the grid was removed from solution and air dried prior to re-examination using the TEM.

ASSOCIATED CONTENT

Supplementary PDF document containing: Transmission Electron Microscopy and Scanning Electron Microscopy images analyzed for particle size distributions, tables with measurement data, additional information on in-situ electrochemical atomic force microscopy experiments, additional information on X-ray adsorption spectroscopy setup, Nuclear Magnetic Resonance data, gas chromatography data, ICP-OES results

AUTHOR INFORMATION

Corresponding author

Juliane Weber - Chemical Sciences Division, Oak Ridge National Laboratory, weberj@ornl.gov
ORCID: 0000-0001-7961-0220

Authors

Seunghoon Lee-Chemical Sciences Division, Oak Ridge National Laboratory, ORCID: 0000-0002-8307-8588

Nishu Devi- Chemical Sciences Division, Oak Ridge National Laboratory, ORCID: 0000-0002-9021-0516

Yuanyuan Li - Chemical Sciences Division, Oak Ridge National Laboratory, ORCID: 0000-0003-3074-9672

Yiqing Wu - Chemical Sciences Division, Oak Ridge National Laboratory, ORCID: 0000-0001-5014-3761

Barbara R. Evans- Chemical Sciences Division, Oak Ridge National Laboratory, ORCID: 0000-0002-2574-2567

Matthew G. Boebinger - Center for Nanophase Materials Sciences, Oak Ridge National Laboratory, ORCID: 0000-0001-9622-2043

Andrew G. Stack - Chemical Sciences Division, Oak Ridge National Laboratory ORCID: 0000-0003-4355-3679

Zili Wu - Chemical Sciences Division, Oak Ridge National Laboratory, Center for Nanophase Materials Sciences, Oak Ridge National Laboratory ORCID: 0000-0002-4468-3240

Notes

The authors declare no competing financial interest.

ACKNOWLEDGMENTS.

This work was primarily supported as part of the Center for Understanding & Controlling Accelerated and Gradual Evolution of Materials for Energy (UNCAGE-ME), an Energy Frontier Research Center funded by the U.S. Department of Energy, Office of Science, Basic Energy Sciences under award no. DE-SC0012577. AGS' contribution on ligand-promoted dissolution was supported by the U.S. Department of Energy, Office of Science, Office of Basic Energy Sciences, Chemical Sciences, Geosciences, and Biosciences Division. The characterization (SEM, TEM and near identical location TEM) was conducted as part of a user project at the Center for Nanophase

Materials Sciences (CNMS), which is a U.S. Department of Energy, Office of Science User Facility at Oak Ridge National Laboratory. This research used resources of the National Synchrotron Light Source II, a U.S. Department of Energy (DOE) Office of Science User Facility operated for the DOE Office of Science by Brookhaven National Laboratory under Contract No. DE-SC0012704. Beamline operations were supported in part by the Synchrotron Catalysis Consortium (U.S. DOE, Office of Basic Energy Sciences, Grant No. DE-SC0012335). Harry Meier is acknowledged for XPS measurements.

References

(1) Lin, Y.; Wang, T.; Zhang, L.; Zhang, G.; Li, L.; Chang, Q.; Pang, Z.; Gao, H.; Huang, K.; Zhang, P.; et al. Tunable CO_2 electroreduction to ethanol and ethylene with controllable interfacial wettability. *Nature Communications* **2023**, *14* (1), 3575. DOI: 10.1038/s41467-023-39351-2.

(2) Popović, S.; Smiljanić, M.; Jovanovič, P.; Vavra, J.; Buonsanti, R.; Hodnik, N. Stability and degradation mechanisms of copper-based catalysts for electrochemical CO_2 reduction. *Angewandte Chemie* **2020**, *132* (35), 14844-14854.

(3) Nitopi, S.; Bertheussen, E.; Scott, S. B.; Liu, X.; Engstfeld, A. K.; Horch, S.; Seger, B.; Stephens, I. E. L.; Chan, K.; Hahn, C.; et al. Progress and Perspectives of Electrochemical CO_2 Reduction on Copper in Aqueous Electrolyte. *Chemical Reviews* **2019**, *119* (12), 7610-7672. DOI: 10.1021/acs.chemrev.8b00705.

(4) Birdja, Y. Y.; Pérez-Gallent, E.; Figueiredo, M. C.; Göttle, A. J.; Calle-Vallejo, F.; Koper, M. T. M. Advances and challenges in understanding the electrocatalytic conversion of carbon dioxide to fuels. *Nature Energy* **2019**, *4* (9), 732-745. DOI: 10.1038/s41560-019-0450-y.

(5) Ummireddi, A. K.; Li, Z.; Wu, J. Copper defects for CO2 electrocatalysis toward a specific multicarbon product. *Trends in Chemistry* **2023**, *5* (3), 170-173.

(6) McCafferty, E. Thermodynamics of Corrosion: Pourbaix Diagrams. In *Introduction to Corrosion Science*, 2010; pp 95-117.

(7) Kim, Y.-G.; Baricuatro, J. H.; Javier, A.; Gregoire, J. M.; Soriaga, M. P. The Evolution of the Polycrystalline Copper Surface, First to Cu(111) and Then to Cu(100), at a Fixed CO_2RR Potential: A Study by Operando EC-STM. *Langmuir* **2014**, *30* (50), 15053-15056. DOI: 10.1021/la504445g.

(8) Manthiram, K.; Beberwyck, B. J.; Alivisatos, A. P. Enhanced electrochemical methanation of carbon dioxide with a dispersible nanoscale copper catalyst. *Journal of the American Chemical Society* **2014**, *136* (38), 13319-13325.

(9) Gunathunge, C. M.; Li, X.; Li, J.; Hicks, R. P.; Ovalle, V. J.; Waegele, M. M. Spectroscopic observation of reversible surface reconstruction of copper electrodes under CO2 reduction. *The Journal of Physical Chemistry C* **2017**, *121* (22), 12337-12344.

(10) Kim, D.; Kley, C. S.; Li, Y.; Yang, P. Copper nanoparticle ensembles for selective electroreduction of CO2 to C2–C3 products. *Proceedings of the National Academy of Sciences* **2017**, *114* (40), 10560-10565.

(11) Grosse, P.; Gao, D.; Scholten, F.; Sinev, I.; Mistry, H.; Roldan Cuenya, B. Dynamic Changes in the Structure, Chemical State and Catalytic Selectivity of Cu Nanocubes during CO_2 Electroreduction: Size and Support Effects. *Angew Chem Int Ed Engl* **2018**, *57* (21), 6192-6197. DOI: 10.1002/anie.201802083 From NLM PubMed-not-MEDLINE.

(12) Grosse, P.; Yoon, A.; Rettenmaier, C.; Herzog, A.; Chee, S. W.; Roldan Cuenya, B. Dynamic transformation of cubic copper catalysts during CO_2 electroreduction and its impact on catalytic selectivity. *Nat Commun* **2021**, *12* (1), 6736. DOI: 10.1038/s41467-021-26743-5 From NLM PubMed-not-MEDLINE.

(13) Simon, G. H.; Kley, C. S.; Roldan Cuenya, B. Potential-Dependent Morphology of Copper Catalysts During CO_2 Electroreduction Revealed by In Situ Atomic Force Microscopy. *Angewandte Chemie International Edition* **2021**, *60* (5), 2561-2568. DOI: https://doi.org/10.1002/anie.202010449.

(14) Vavra, J.; Shen, T. H.; Stoian, D.; Tileli, V.; Buonsanti, R. Real-time Monitoring Reveals Dissolution/Redeposition Mechanism in Copper Nanocatalysts during the Initial Stages of the CO_2 Reduction Reaction. *Angew Chem Int Ed Engl* **2021**, *60* (3), 1347-1354. DOI: 10.1002/anie.202011137 From NLM PubMed-not-MEDLINE.

(15) Lee, S. H.; Lin, J. C.; Farmand, M.; Landers, A. T.; Feaster, J. T.; Avilés Acosta, J. E.; Beeman, J. W.; Ye, Y.; Yano, J.; Mehta, A.; et al. Oxidation State and Surface Reconstruction of Cu under CO_2 Reduction Conditions from In Situ X-ray Characterization. *Journal of the American Chemical Society* **2021**, *143* (2), 588-592. DOI: 10.1021/jacs.0c10017.

(16) Cherevko, F. D. S. S. Electrochemical copper dissolution: A benchmark for stable CO2 reduction on copper electrocatalysts. *Electrochemistry Communications* **2020/06/01**, *115*, 106739. DOI: 10.1016/j.elecom.2020.106739.

(17) Takamatsu, D.; Fukatani, N.; Yoneyama, A.; Hirano, T.; Hirai, K.; Yabuuchi, S.; Watanabe, K.; Kamiya, K.; Nakanishi, S. Dynamic Relocation of Copper Catalysts in Gas Diffusion Electrodes during CO2 Electroreduction. *Journal of the American Chemical Society* **June 25, 2025**. DOI: 10.1021/jacs.5c07944.

(18) Tomc, B.; Tomc, B.; Bele, M.; Bele, M.; Nazrulla, M. A.; Nazrulla, M. A.; Šket, P.; Šket, P.; Finšgar, M.; Finšgar, M.; et al. Deactivation of copper electrocatalysts during CO2 reduction

occurs via dissolution and selective redeposition mechanism. *Journal of Materials Chemistry A* **2025/02/04**, *13* (6). DOI: 10.1039/D4TA06466F.

(19) Lee, S. H.; Avilés Acosta, J. E.; Lee, D.; Larson, D. M.; Li, H.; Chen, J.; Lee, J.; Erdem, E.; Lee, D. U.; Blair, S. J. Structural Transformation and Degradation of Cu Oxide Nanocatalysts during Electrochemical CO2 Reduction. *Journal of the American Chemical Society* **2025**.

(20) Jung, H.; Lee, S. Y.; Lee, C. W.; Cho, M. K.; Won, D. H.; Kim, C.; Oh, H.-S.; Min, B. K.; Hwang, Y. J. Electrochemical fragmentation of Cu2O nanoparticles enhancing selective C–C coupling from CO2 reduction reaction. *Journal of the American Chemical Society* **2019**, *141* (11), 4624-4633.

(21) Huang, J.; Hörmann, N.; Oveisi, E.; Loiudice, A.; De Gregorio, G. L.; Andreussi, O.; Marzari, N.; Buonsanti, R. Potential-induced nanoclustering of metallic catalysts during electrochemical CO_2 reduction. *Nature communications* **2018**, *9* (1), 3117.

(22) Hori, Y.; Konishi, H.; Futamura, T.; Murata, A.; Koga, O.; Sakurai, H.; Oguma, K. "Deactivation of copper electrode" in electrochemical reduction of CO2. *Electrochimica acta* **2005**, *50* (27), 5354-5369.

(23) Vavra, J.; Ramona, G. P. L.; Dattila, F.; Kormányos, A.; Priamushko, T.; Albertini, P. P.; Loiudice, A.; Cherevko, S.; Lopéz, N.; Buonsanti, R. Solution-based Cu+ transient species mediate the reconstruction of copper electrocatalysts for CO_2 reduction. *Nature Catalysis* **2024**, *7* (1), 89-97. DOI: 10.1038/s41929-023-01070-8.

(24) Eren, B.; Zherebetskyy, D.; Patera, L. L.; Wu, C. H.; Bluhm, H.; Africh, C.; Wang, L.-W.; Somorjai, G. A.; Salmeron, M. Activation of Cu(111) surface by decomposition into nanoclusters driven by CO adsorption. *Science* **2016**, *351* (6272), 475-478. DOI: doi:10.1126/science.aad8868.

(25) Amirbeigiarab, R.; Tian, J.; Herzog, A.; Qiu, C.; Bergmann, A.; Roldan Cuenya, B.; Magnussen, O. M. Atomic-scale surface restructuring of copper electrodes under CO2 electroreduction conditions. *Nature Catalysis* **2023**, *6* (9), 837-846.

(26) Xu, L.; Lin, J.; Bai, Y.; Mavrikakis, M. Atomic and molecular adsorption on Cu (111). *Topics in Catalysis* **2018**, *61*, 736-750.

(27) Vollmer, S.; Witte, G.; Wöll, C. Determination of site specific adsorption energies of CO on copper. *Catalysis letters* **2001**, *77*, 97-101.

(28) Materials Data on Cu by Materials Project. LBNL Materials Project; Lawrence Berkeley National Laboratory (LBNL), B., CA (United States), Ed.; 2020.

(29) Materials Data on Cu2O by Materials Project. LBNL Materials Project; Lawrence Berkeley National Laboratory (LBNL), B., CA (United States), Ed.; 2020.

(30) Ma, D.; Zhi, C.; Zhang, Y.; Chen, J.; Zhang, Y.; Shi, J.-W. A Review on the Influence of Crystal Facets on the Product Selectivity of CO2RR over Cu Metal Catalysts. *ACS nano* **2024**, *18* (33), 21714-21746.

(31) Quan, Z.; Wang, Y.; Fang, J. High-index faceted noble metal nanocrystals. *Accounts of Chemical Research* **2013**, *46* (2), 191-202.

(32) Durand, W. J.; Peterson, A. A.; Studt, F.; Abild-Pedersen, F.; Nørskov, J. K. Structure effects on the energetics of the electrochemical reduction of CO2 by copper surfaces. *Surface Science* **2011**, *605* (15-16), 1354-1359.

(33) Han, C.; Kundi, V.; Ma, Z.; Toe, C. Y.; Kumar, P.; Tsounis, C.; Jiang, J.; Xi, S.; Han, Z.; Lu, X. Differentiating the Impacts of Cu2O Initial Low-and High-Index Facets on Their Reconstruction and Catalytic Performance in Electrochemical CO2 Reduction Reaction. *Advanced Functional Materials* **2023**, *33* (12), 2210938.

(34) Huang, H.; Yue, K.; Liu, C.; Zhan, K.; Dong, H.; Yan, Y. CuO (111) Microcrystalline evoked indium–organic framework for efficient electroreduction of CO_2 to formate. *Small* **2024**, *20* (34), 2400441.

(35) Zhong, W.; Chi, Y.; Yu, R.; Kong, C.; Zhou, S.; Han, C.; Vongsvivut, J.; Mao, G.; Kalantar-Zadeh, K.; Amal, R. Liquid Metal-Enabled Tunable Synthesis of Nanoporous Polycrystalline Copper for Selective CO_2-to-Formate Electrochemical Conversion. *Small* **2024**, *20* (49), 2403939.

(36) Rahaman, M.; Dutta, A.; Zanetti, A.; Broekmann, P. Electrochemical reduction of CO_2 into multicarbon alcohols on activated Cu mesh catalysts: an identical location (IL) study. *ACS Catalysis* **2017**, *7* (11), 7946-7956.

(37) Scott, S. B.; Hogg, T. V.; Landers, A. T.; Maagaard, T.; Bertheussen, E.; Lin, J. C.; Davis, R. C.; Beeman, J. W.; Higgins, D.; Drisdell, W. S. Absence of oxidized phases in Cu under CO reduction conditions. *ACS Energy Letters* **2019**, *4* (3), 803-804.

(38) Reske, R.; Mistry, H.; Behafarid, F.; Roldan Cuenya, B.; Strasser, P. Particle size effects in the catalytic electroreduction of CO2 on Cu nanoparticles. *Journal of the American Chemical Society* **2014**, *136* (19), 6978-6986.

(39) Ludwig, C.; Casey, W. H.; Rock, P. A. Prediction of ligand-promoted dissolution rates from the reactivities of aqueous complexes. *Nature* **1995**, *375* (6526), 44-47.

(40) Holmén, B. A.; Casey, W. H. Hydroxamate ligands, surface chemistry, and the mechanism of ligand-promoted dissolution of goethite [α-FeOOH (s)]. *Geochimica et Cosmochimica Acta* **1996**, *60* (22), 4403-4416.

(41) Furrer, G.; Stumm, W. The coordination chemistry of weathering: I. Dissolution kinetics of δ-Al2O3 and BeO. *Geochimica et Cosmochimica Acta* **1986**, *50* (9), 1847-1860.

(42) Molis, E.; Barres, O.; Marchand, H.; Sauzéat, E.; Humbert, B.; Thomas, F. Initial steps of ligand-promoted dissolution of gibbsite. *Colloids and Surfaces A: Physicochemical and Engineering Aspects* **2000**, *163* (2-3), 283-292.

(43) Heliövaara, E.; Liljeqvist, H.; Muuronen, M.; Eronen, A.; Moslova, K.; Repo, T. Cooperative Ligands in Dissolution of Gold. *Chemistry–A European Journal* **2021**, *27* (34), 8668-8672.

(44) Guan, Y.; Kümper, J.; Mürtz, S. D.; Kumari, S.; Hausoul, P. J.; Palkovits, R.; Sautet, P. Origin of copper dissolution under electrocatalytic reduction conditions involving amines. *Chemical Science* **2024**, *15* (35), 14485-14496.

(45) Liu, S.; Liu, Y.; Pan, B.; He, Y.; Li, B.; Zhou, D.; Xiao, Y.; Qiu, H.; Vijver, M. G.; Peijnenburg, W. J. The promoted dissolution of copper oxide nanoparticles by dissolved humic acid: Copper complexation over particle dispersion. *Chemosphere* **2020**, *245*, 125612.

(46) Hori, Y.; Murata, A.; Takahashi, R. Formation of hydrocarbons in the electrochemical reduction of carbon dioxide at a copper electrode in aqueous solution. *Journal of the Chemical Society, Faraday Transactions 1: Physical Chemistry in Condensed Phases* **1989**, *85* (8), 2309-2326.

(47) DeWulf, D. W.; Jin, T.; Bard, A. J. Electrochemical and surface studies of carbon dioxide reduction to methane and ethylene at copper electrodes in aqueous solutions. *Journal of the Electrochemical Society* **1989**, *136* (6), 1686.

(48) Feaster, J. T.; Shi, C.; Cave, E. R.; Hatsukade, T.; Abram, D. N.; Kuhl, K. P.; Hahn, C.; Nørskov, J. K.; Jaramillo, T. F. Understanding Selectivity for the Electrochemical Reduction of Carbon Dioxide to Formic Acid and Carbon Monoxide on Metal Electrodes. *ACS Catalysis* **2017**, *7* (7), 4822-4827. DOI: 10.1021/acscatal.7b00687.

(49) Guan, Y.; Guan, Y.; Kümper, J.; Kümper, J.; Mürtz, S. D.; Mürtz, S. D.; Kumari, S.; Kumari, S.; Hausoul, P. J. C.; Hausoul, P. J. C.; et al. Origin of copper dissolution under electrocatalytic reduction conditions involving amines. *Chemical Science* **2024/09/11**, *15* (35). DOI: 10.1039/D4SC01944J.

(50) V.N. Krasil'nikov, V. P. Z., E.V. Chulkov, I.V. Baklanova, D.G. Kellerman, O.I. Gyrdasova, ; T.V. Dyachkova, A. P. T. Novel method for the production of copper(II) formates, their thermal, spectral and magnetic properties. *Journal of Alloys and Compounds* **2020/12/10**, *845*. DOI: 10.1016/j.jallcom.2020.156208.

(51) C. M. Pradier*, a.; Dubot‡, P. Adsorption and Reactivity of Sulfur Dioxide on Cu(110). Influence of Oxidation and Hydroxylation of the Surface. **June 6, 1998**. DOI: 10.1021/jp981000.

(52) Polčik, M.; Wilde, L.; Haase, J. ${\mathrm{SO}}_{2}$-induced surface reconstruction of Cu(111): An x-ray-absorption fine-structure study. *Physical Review B* **1998-01-15**, *57* (3). DOI: 10.1103/PhysRevB.57.1868.

(53) Leung, K. T.; Zhang, X. S.; Shirley, D. A. Adsorption and surface reactions of hydrogen sulfide and sulfur dioxide on copper(100) studied by electron energy loss spectroscopy. **May 1, 2002**. DOI: 10.1021/j100353.

(54) Alemozafar, A. R.; , X.-C. G., Robert J. Madix. Topographic nano-restructuring: sulfur dioxide adsorption on Cu(110). *Surface Science* **2003/02/01**, *524* (1-3). DOI: 10.1016/S0039-6028(02)02539-6.

(55) Behjatmanesh-Ardakani, R.; Magkoev, T. T. SO2 adsorption and its direct proportional dissociation on the Cu(100), Cu(110), and Cu(111) surfaces: a periodic DFT study. *Chemical Review and Letters* **2024/11/01**, *7* (5). DOI: 10.22034/crl.2024.467740.1380.

(56) Luc, W.; Ko, B. H.; Kattel, S.; Li, S.; Su, D.; Chen, J. G.; Jiao, F. SO_2-induced selectivity change in CO_2 electroreduction. *Journal of the American Chemical Society* **2019**, *141* (25), 9902-9909.

(57) Giovannelli, G.; Natali, S.; Zortea, L.; Bozzini, B. An investigation into the surface layers formed on oxidised copper exposed to SO_2 in humid air under hypoxic conditions. *Corrosion science* **2012**, *57*, 104-113.

(58) Hatab, A. S. A.; Ahmad, Y. H.; Mady, M. F.; Hassan, Y.; Zkria, A.; Sinopoli, A.; Abdullah, A. M.; Al-Qaradawi, S. Y.; Yoshitake, T.; Khaled, M. Nuclear magnetic resonance spectroscopy: A comprehensive tool for analyzing liquid products in electrochemical CO2 reduction. *Journal of Electroanalytical Chemistry* **2025**, *986*, 119097.

(59) Cheng, D.; Nguyen, K.-L. C.; Sumaria, V.; Wei, Z.; Zhang, Z.; Gee, W.; Li, Y.; Morales-Guio, C. G.; Heyde, M.; Roldan Cuenya, B. Structure sensitivity and catalyst restructuring for CO2 electro-reduction on copper. *Nature Communications* **2025**, *16* (1), 4064.

(60) Ravel, B.; Newville, M. ATHENA, ARTEMIS, HEPHAESTUS: data analysis for X-ray absorption spectroscopy using IFEFFIT. *Synchrotron Radiation* **2005**, *12* (4), 537-541.

773 **Table of Content Graphic**

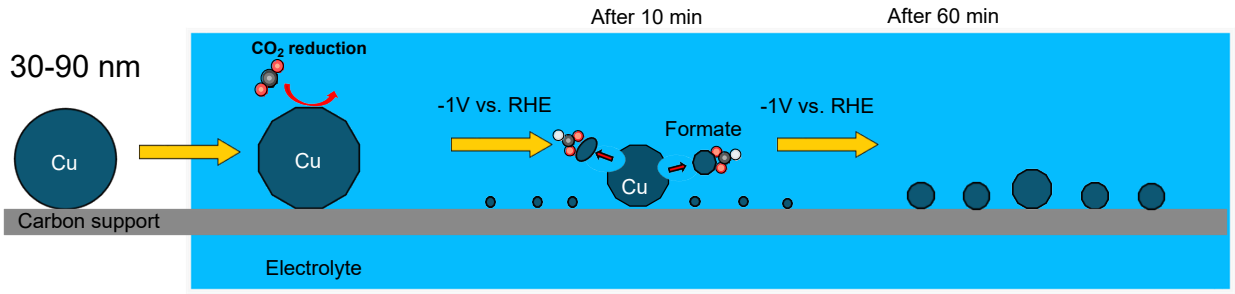

(2) Strong binding of formic acid intermediate

(3) Small growth of the small and new NPs (20-60 nm)

774

775